NANO LETTERS

pubs.acs.org/NanoLett

Letter

Flexible Tactile Sensors for 3D Force Detection

Chengcheng Han, Zhi Cao, Yiran Hu, Zhiwei Zhang, Chengyu Li, Zhong Lin Wang,* and Zhiyi Wu*

Cite This: *Nano Lett.* 2024, 24, 5277−5283

Read Online

ACCESS | Metrics & More | Article Recommendations | Supporting Information

ABSTRACT: As tactile force sensing has become increasingly significant in the field of machine haptics, achieving multidimensional force sensing remains a challenge. We propose a 3D flexible force sensor that consists of an axisymmetric hemispherical protrusion and four equally sized quarter-circle electrodes. By simulating the device using a force and electrical field model, it has been found that the magnitude and direction of the force can be expressed through the voltage relationship of the four electrodes when the magnitude of the shear force remains constant and its direction varies within 0−360°. The experimental results show that a resolution of 15° can be achieved in the range 0−90°. Additionally, we installed the sensor on a robotic hand, enabling it to perceive the magnitude and direction of touch and grasp actions. Based on this, the designed 3D flexible tactile force sensor provides valuable insights for multidimensional force detection and applications.

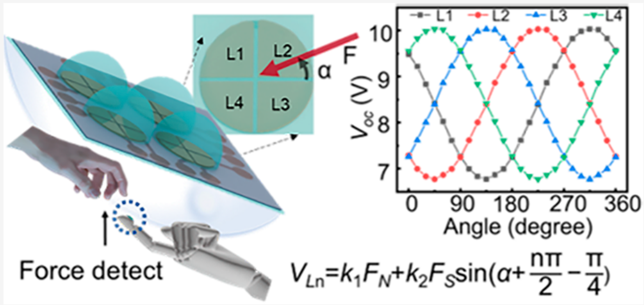

KEYWORDS: *flexible tactile sensing, single-electrode mode, force detection, normal and shear forces, robotic hand system*

With the rapid development of technology, tactile sensors are increasingly being used in fields such as intelligent robotics,[1−5] biomimetic prosthetics,[6−8] and human−machine interaction.[9−11] For example, the use of intelligent robots to interact with patients during the COVID-19 pandemic has effectively reduced the risk of cross-infection. Flexible tactile sensors, as a crucial component of intelligent robots, are essential for performing tasks that require high dexterity, such as grabbing, holding, and touching.[12,13] These tactile sensors can detect a variety of tactile stimuli, including presses, knocks, and slides.[14−16] Tactile sensing is crucial for enabling robots to perceive objects,[17−20] with the detection of forces being particularly important. To date, there have been many reports focusing on designing microstructures and improving sensing materials to increase the sensitivity of force sensors.[21−23] The majority of sensors react to unidirectional forces, but in actual use, being able to recognize normal and shear forces is essential.[24−29] Therefore, a tactile sensor that can sense both the magnitude and direction of force is an inspiring and challenging research issue.

In recent years, numerous studies have investigated various kinds of tactile sensors based on piezoresistive, capacitive, piezoelectric, and triboelectric processes to address these challenges.[30−35] Among these, triboelectric nanogenerators (TENGs) can not only directly convert mechanical motion into electrical energy but also offer advantages such as a diverse selection of materials, high voltage signals, high sensitivity, and simplicity in fabrication.[36,37] Although force tactile sensors play a crucial role in practical applications,[34,38] most force sensors can only measure normal forces,[39] and the shear force components with direction information are rarely studied by TENG-based sensors. This greatly limits their application in robotic tasks involving complex multidimensional force states.[40−42] Based on this, in this study we focus on the design of a flexible tactile sensor structure based on triboelectric nanogenerators for detecting both normal and shear forces.

Here, we report on a multidimensional flexible tactile sensor based on a single-electrode mode TENG, featuring an axisymmetric hemispherical protrusion and four equally sized quarter-circle electrodes. For normal force sensing, its detection range is 0−10 N. Subsequently, simulations of the device showed that the magnitude and direction of force can be indicated by the voltage relationship of the four electrodes when the shear force is constant, and its direction varies within a 0−360° range. Experimentally, the device has the ability to resolve the direction of the shear force with a resolution of 15°. Moreover, we installed the flexible tactile sensor array on the robotic hand's surface, enabling it to perceive the magnitude and direction of forces. This further demonstrates the significant potential of flexible multidimensional tactile sensor arrays in human−machine interaction applications.

Received: February 20, 2024
Revised: April 7, 2024
Accepted: April 11, 2024
Published: April 16, 2024

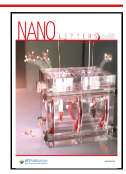

https://doi.org/10.1021/acs.nanolett.4c00894
Nano Lett. 2024, 24, 5277−5283

We present a streamlined manufacturing process for flexible tactile sensor arrays (Figure 1a), comprising a flexible contact

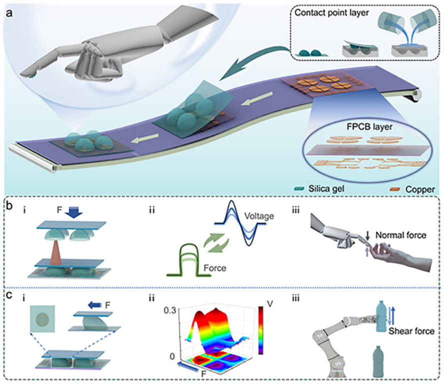

Figure 1. (a) Flowchart of the preparation of the 3-dimensional flexible tactile sensor. (b) (i) Schematic diagram of the response of the flexible tactile sensor to the normal force. (ii) Relationship between the normal force and the output of the V_{oc}. (iii) Schematic diagram of the application of normal force detection in human–computer interaction. (c) (i) Schematic diagram of the response of the flexible tactile sensor to the shear force. (ii) Situation of the output response of the tactile sensor under a certain shear force. (iii) Schematic diagram of the application of shear force detection in the robotic hand gripping process.

and a FPCB (flexible printed circuit board) layer, detailed in the Materials and Methods section and Figure S1a,b. Initially, a 2-by-2 sensor unit array template is created via 3D printing. Then, a silicon solution is poured into the template for full coverage and allowed to air-dry at room temperature, forming a peelable flexible point array structure, as shown in Figure 1a, upper right. The SEM image in Figure S1c shows the silicone contact's surface with uniform microstripes, enhancing friction and TENG output. The device's FPCB features 16 quarter-copper-pad electrodes, 3 mm in diameter, and a structure with a top copper electrode, a perforated polyimide center, and a copper solder joint bottom (Figure 1a, lower right). Demonstrating its application, we attached the flexible tactile sensor to a manipulator for detecting normal and shear forces, with images in Figure S2.

In detail, Figure 1b-i shows the tactile sensor array's response to normal force, transitioning from point to face contact as pressure increases, enlarging the contact area. In Figure 1b-ii, the increased contact area boosts charge induction and output signal from the nanogenerator's electrode layer. This sensitivity to slight forces enhances TENG-based sensors with hemispherical contacts' force detection. Figure 1b-iii demonstrates its application in sensing normal forces on robot hands for human–machine interaction.

To detect the force magnitude and direction, we designed a sensor with four quarter-circle electrodes under a silicone hemisphere. This setup lets the device discern forces of different magnitudes and directions by analyzing changes in the electrodes' outputs. Nonvertical forces or sliding creates asymmetric contact area changes, affecting the electrodes differently.

As shown in Figure 1c-i, when the contact is subjected to a force to the left, the contact area change generated by tilting the contact to the left is more concentrated on the left side, causing the left electrode to sense more charge than the right

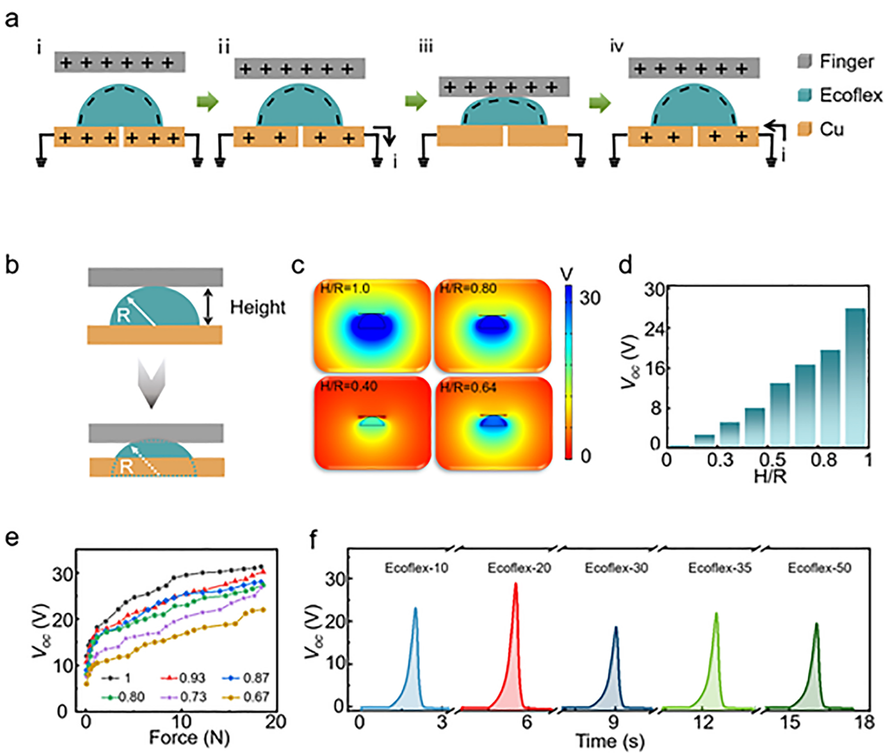

Figure 2. (a) Working schematic diagram of one contact of the tactile sensor during one press. (b) Schematic diagram of silicone contact with radius R and H/R at different heights H. (c) Simulated potential diagrams of silicone contact with H/R at different heights H for a radius R. (d) Silicone contact voltage data plot for various H/R. (e) V_{oc} change values of silicone contact with different H/R at different forces. (f) V_{oc} waveform data graphs for different silicone model types.

https://doi.org/10.1021/acs.nanolett.4c00894
Nano Lett. 2024, 24, 5277−5283

electrode, as illustrated in Figure 1c-ii. By analyzing and comparing the differences in the output signals of the four electrodes are analyzed and compared, the magnitude and direction of the applied force can be inferred. Furthermore, the tactile sensor can be used on a robotic hand surface, as demonstrated in Figure 1c-iii. During the process of the robotic hand gripping a bottle, shear forces occur, and by detecting these forces, the state of the robotic hand's grip can be ascertained.

Figure 2a illustrates the working principle of the flexible tactile sensor combining contact electrification and electrostatic induction. Initially, the separation distance between the silicone and the finger is at a maximum, inducing the most charge on the bottom electrode (Figure 2a-i). As the hand approaches and compresses the silicone protrusion, the potential difference between them decreases, and the induced charge on the bottom decreases accordingly (Figure 2a-ii). At maximum compression of the silicone by hand, the induced charge is minimal (Figure 2a-iii), returning to its initial values when the finger retracts. This process results in changes in the potential difference, and the force applied by the hand, both its magnitude and direction, causes corresponding changes in the voltage across the four electrodes. By analyzing the voltage output of the four electrodes, the magnitude and direction of the force can be inferred.

We explored how the silicone contact's H/R ratio affects output voltage by testing different H values at a constant R under the same pressure (Figures 2b). COMSOL simulations showed potential distribution varies with H/R, with higher voltage at H/R = 1 due to larger contact area and uniform pressure distribution enhancing charge transfer (Figures 2c,d). Experiments confirmed the highest V_{oc} output at H/R = 1, indicating hemispherical contacts with this ratio optimize performance (Figure 2e). Thus, we used a silicone hemisphere with H/R = 1 for further studies, leveraging its effective charge transfer and uniform pressure distribution benefits. Beyond the silicone contact shape, we investigated the impact of silicone types on device output, finding Ecoflex-20 delivered the highest V_{oc} under 10 N pressure (Figure 2f). Its superior flexibility and robustness likely contributed to this performance. Consequently, we selected Ecoflex-20 with an H/R ratio of 1 for further experiments, based on its optimal output characteristics.

We designed 3 mm radius silicone contacts to shrink the 3D tactile force sensor to a finger-sized, practical form for the robotic hand. We initially analyzed the sensor's response to normal forces, focusing on the deformation of the silicone contact points and the voltage output (V_{oc}) from the bottom electrodes. Figure 3a shows the contact flattening and deforming under a specific normal force. As illustrated on the left side of Figure 3b, the average amount of deformation of the contact point under a particular amount of normal force is simulated using COMSOL. The image shows that when the normal force gradually increases, the average contact point deformation also gradually increases and the potential of the bottom electrode is also increasing, as indicated on the right side of Figure 3b, and the detailed process refers to Video S1. The results of the simulation are depicted in Figure 3c.

In experiments, a 3 N force produced 0.6 V across four electrodes, as 3D plotted in Figure 3d. Figure 3e and Figure S3 show V_{oc} rises with pressure to 0.9 V at 9 N, with sensitivities of 0.25 V/N under 2.4 N and 0.033 V/N for 2.4−10 N, when the contact point is continuously subjected to a normal force,

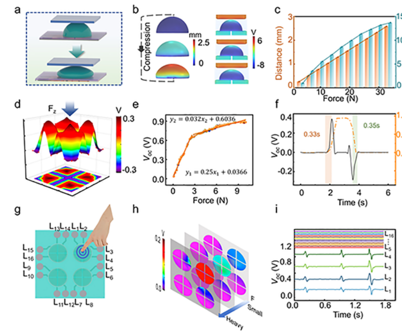

Figure 3. (a) Schematic diagram of a device for testing normal force. (b) Simulation plots of the average amount of shape change and potential during the movement of a single contact point under different normal forces. (c) Simulation plots of the average amount of displacement change and potential during the movement of a single silicone contact under normal forces. (d) 3D data plots of the V_{oc} under a pressure of 5 N. (e) Relationship between the positive pressure and the amplitude of the output V_{oc} with the fitting straight line. (f) Response and recovery times of the silicone contact under a normal force of 5 N. (g) Schematic diagram of finger pressing with different normal forces. (h) Real-time data plot of finger pressing with different normal forces. (i) Real-time V_{oc} waveform of finger pressing with different normal forces.

and the potential induced by the bottom electrode also exhibits a gradually increasing trend. This change reflects the shift in the contact region's position between the upper contact and lower electrode under force.

Upon increasing the normal force, the contact area and electrode-generated charge rise, enhancing V_{oc}. However, increased stiffness at higher forces limits contact area expansion, reducing measurement sensitivity. The sensor demonstrates response and recovery times of 0.33 and 0.35 s, respectively, for practical application viability, as shown in Figure 3f. These times are sufficient despite not reaching millisecond speed due to object movement constraints. Further, we characterized the output of the entire flexible tactile sensor under applied normal force. After examining individual contacts, we analyzed the outputs of 16 electrodes from four silicone contacts (Figure 3g). Real-time V_{oc} mapping under varying finger pressures is shown in Figure 3h, detailed in Video S2. V_{oc} waveforms in Figure 3i reveal that V_{oc} increases with pressure. Crucially, Figure S4 shows minimal interference among electrodes, with only the targeted electrode output upon pressure. Durability tests in Figure S5 show that V_{oc} remained stable (0.82 to 0.81 V) after 6000 cycles, proving the sensor's reliability and mechanical endurance.

Afterward, we analyzed the voltage of the device under shear forces. First, we used COMSOL for simulation analysis of the device, with the simulation model shown in Figure 4a. Equal and opposite charges Q were applied to the contact object and the upper surface of the silicone. The locations of the four electrodes in the model are located in the bottom right corner. The deformation simulation results, as shown in Figure 4b, indicate that as the magnitude of the force increases while its direction remains constant, the deformation of the contact point also gradually rises. The obtained four electrode voltage simulation results are shown in Figure S6. In order to better investigate the voltage outputs of the four electrodes under various shear force directions, keeping the force magnitude at 10 N and θ at 30°constant, only changing the angle α from 0° to 90°, the voltage data of the four electrodes are presented in

https://doi.org/10.1021/acs.nanolett.4c00894
Nano Lett. 2024, 24, 5277−5283

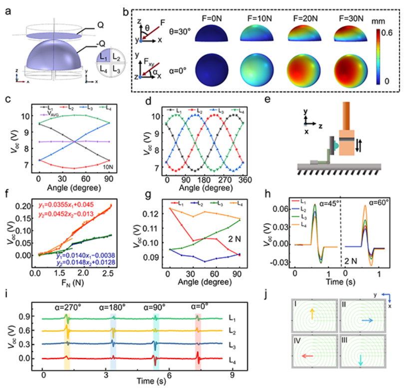

Figure 4. (a) Schematic diagram of the charge on the lower surface of the object and the surface of the silicone contact. (b) Simulation of the average deformation amount during the motion process of a single contact point under different pressures. (c) V_{oc} of four electrodes and the average voltage data curve for shear force α at 0−90°. (d) V_{oc} of four electrodes for shear force α at 0−360°. (e) Schematic diagram of the device's shear force test. (f) V_{oc} of four electrodes under different pressures and shear force directions. (g) V_{oc} of four electrodes under 2 N shear in different shear force directions. (h) V_{oc} of four electrodes under 2 N shear force at 45° and 60° shear force directions. (i) V_{oc} of four electrodes in shear force direction application test under different α angles. (j) Schematic diagram of four shear force directions.

Figure 4c, where V_{AVG} represents the average value obtained after summing up the four voltages.

$$V_{AVG} = \frac{V_{L_1} + V_{L_2} + V_{L_3} + V_{L_4}}{4} \tag{1}$$

The outputs of L_3 and L_4 exhibit an increasing trend as the angle increases from 0°, while the L_1 and L_2 show a decreasing trend. The outputs are equal when = 45° because the corresponding contacts on the L_1 and L_3 electrodes are deformed in a symmetrical manner. As increases, however, the outputs of L_1 and L_4 progressively decrease while those of L_2 and L_3 gradually increase. In particular, when α = 0°, the outputs of L_1 and L_4 are equal and the outputs of L_2 and L_3 are equal; when α = 90°, the outputs of L_3 and L_4 are equal and the outputs of L_1 and L_2 are equal. Furthermore, we can see that V_{AVG} does not change with the direction (α) of the shear force. Furthermore, we simulated the outputs of the four electrodes with different α angles under different shear forces. In order to better analyze the voltage variation between the four electrodes at different angles α, the shear force angle α value in the simulation condition was extended to the range of (0−360°) according to the symmetric relationship between the four electrodes. Figure 4d displays the voltage curve for each of the four electrodes. Moreover, the following formulas can be used to represent the above curves, where n = 1−4:

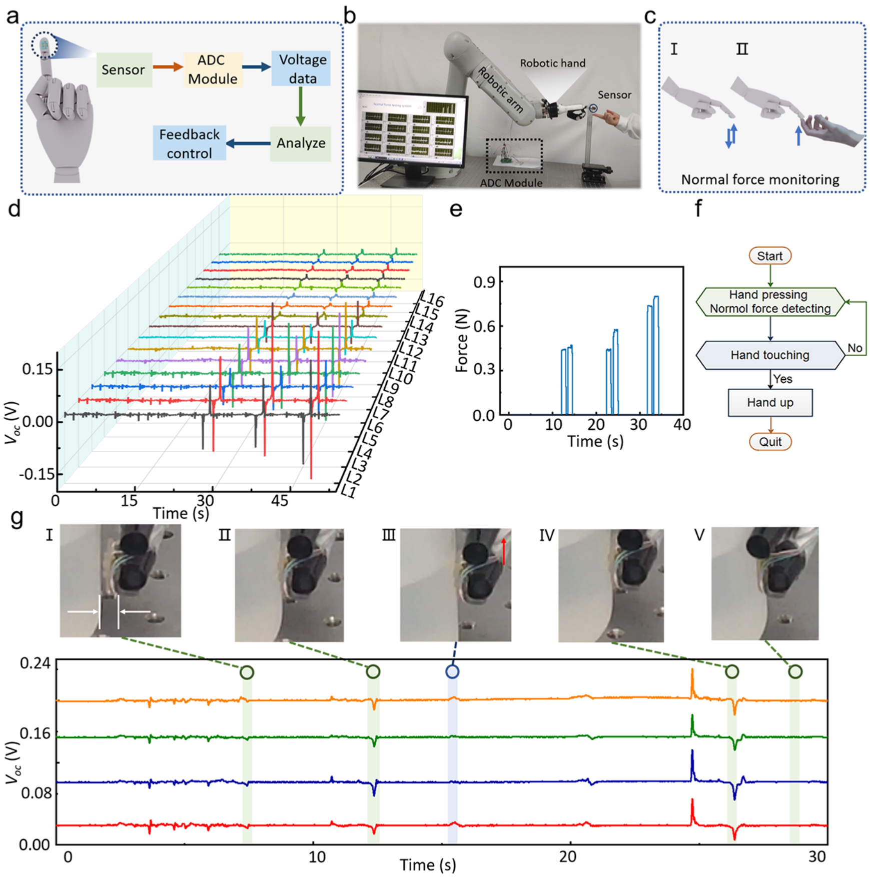

Figure 5. (a) Flow chart of shear and normal forces detected by tactile sensor in robotic hand operating system. (b) A physical drawing of the device for normal force testing. (c) Diagram of the normal force test procedure. (d) The V_{oc} waveforms during normal force test process. (e) The normal force data calculated during test process. (f) Robotic hand-assisted control system with normal force feedback. (g) The V_{oc} of four electrodes in test I−V process.

https://doi.org/10.1021/acs.nanolett.4c00894
Nano Lett. 2024, 24, 5277−5283

$$V_{L_n} = k_1 F_N + k_2 F_S \sin\left(\alpha + \frac{n\pi}{2} - \frac{\pi}{4}\right) \quad (2)$$

As a result, we can use the four electrode voltage equations to separate the normal (F_N) and shear forces (F_S). The detailed decoupling method is shown in Note S1 and Figures S7−S8.

As an illustration, in the flexible tactile sensor array, taking a sensing unit as an example, the sensor is mounted on a 3D displacement platform and moved up and down by a linear motor to study the effect of shear force of different sizes and directions on the device output as shown in Figure 4e. The V_{oc} values of the four electrodes under different shear forces measured during the experiment are shown in Figure 4f. From the image, we can see the slight difference between the outputs of electrodes 1 and 4 and the slight difference between the outputs of electrodes 2 and 3. Then, we selected the V_{oc} of electrodes 1 and 2 for fitting. Among them, the output of electrode 1 is divided into two linear regions with sensitivities of 0.0355 and 0.0452 V/N, respectively, and the outputs of electrode 2 are 0.0140 and 0.0148 V/N, respectively. The detailed V_{oc} of the four electrodes and the slopes of the fitted straight lines are shown as Figure S9. Through experiments, we examined the V_{oc} at different directions of α under 2 N shear force, and the change rule is essentially the same as that of the simulation results as shown in Figure 4g. Specifically, we plotted the V_{oc} waveforms of the four electrodes at $\alpha = 45°$ and $\alpha = 60°$ as shown in Figure 4h. Among these, it can be observed more obviously from the waveforms that when $\alpha = 45°$, the V_{oc} waveforms of L_1 and L_3 are identical. Additionally, we fixed θ and α and varied F to test the voltage of the four electrodes (Figure S10). The experimental results showed that the amplitude A has the same trend with the force as the simulation results. As a single contact shear force application display specific as shown in Video S3, we collect the contact below the four electrodes of the open-circuit voltage for judgment; the judgment is based on the above-mentioned direction of the shear force and the change rule of the open-circuit voltage. Figure 4i shows 270°, 180°, 90°, and 0° of the open-circuit voltage output. Specifically, the size and direction images of the four directions in the application process are shown in Figure 4j.

We affixed the flexible tactile sensing array to the robotic hand for sensing normal and shear force. The output feedback produced by the force between the tactile sensor and object was used to control the robot to perform a closed-loop sensing control system (Figure 5a).

The sensor is connected to the ADC module (Figure S11), and the obtained V_{oc} data are analyzed using LabVIEW software. The physical experimental device is depicted in Figure 5b. Additionally, the normal force application is shown in Figure 5c: the robotic arm moves in an up-and-down cycle unless the sensor detects that the normal force exceeds a threshold, and it will halt its movement and lift. The tactile sensor on the robotic hand generates voltages upon three contacts with the human hand, as shown in Figure 5d. The corresponding calculated forces are depicted in Figure 5e. The entire detection process is illustrated in Figure 5f and demonstrated in Video S4.

Similarly, when the manipulator grips a bottle, the detecting shear force leads to tighter gripping until successful. A flowchart for shear force detection is shown in Figure S12 and is demonstrated in Video S5. Initially, the arm moves from P_0 to P_1, collecting V_{oc} data from tactile sensors for pressure analysis. If the normal force is below a threshold, the arm bends further until it exceeds this value. Then, it moves from P_1 to P_2, analyzing shear force from V_{oc} readings. If the shear force exceeds the threshold, then the arm adjusts until no sliding is detected, indicating a successful grip. The object is then moved back to P_0, completing the task.

To clearly analyze the entire process, we selected the V_{oc} from the four electrodes that are in relatively clear contact the water bottle during the grasping process for analysis, as shown in Figure 5g. The waveforms for the full set of 16 electrodes are displayed in Figure S13. The downward V_{oc} generated in the I and II stages is the analysis of the sensor V_{oc} during the robotic hand's bending. In the I stage, there is a minor bend, and in the II stage, a further bend is observed. It can be seen that the output in the second stage is greater than that in the first, calculating that the force on the finger exceeds the set threshold value. Then, the robotic arm moved upward while analyzing the V_{oc} signals collected, as seen in the III stage. Because of the output generated from sliding exceeding the threshold, the object is not grasped securely. Thus, the robotic arm moved downward, returning to the judgment based on the normal force, allowing the robotic hand to bend further while analyzing the collected V_{oc}, as seen in the IV stage. This concluded that the normal force was greater than the threshold; therefore, the robotic arm moved upward and conducted V_{oc} analysis to determine if the shear was below the threshold. The result is shown in the V stage, where no sliding occurred during the upward movement, meaning the robotic hand successfully grasped the object. Subsequently, under program control, the object is moved to the designated position.

A multi-dimensional flexible tactile sensor based on a single electrode mode TENG is proposed and investigated with a theoretical model, experimental characterization, and application demonstration. In detecting the normal force, it displays two linear ranges in the range of 0−10 N. According to the simulation results, the voltage relationship between the four electrodes can be used to represent both the shear force's magnitude and direction when the force's magnitude is constant and its direction varies within a range of 0−360°, and the resolution is 15° for shear force detection. Furthermore, integration of our sensor into a robot's hand surface enables perception of force direction and strength, showcasing potential for human−computer interaction applications.

The flexible tactile sensor was made using a layered technique, starting with 3D printed templates of four contact patterns, heights at 5 and 3 mm, and 1 mm spacing. Ecoflex silicone (00-10 to 00-50 series) was mixed equally, poured into templates for coverage, degassed under a vacuum, and dried at room temperature. Electrode FPCBs (14.2 × 14.2 mm^2, 0.12 mm thick) were supplied by Huizhou Jiachen Electronic Technology Co., Ltd. The assembly involved attaching the silicone contacts to the FPCB with silicone adhesive (Conibond KN300), as depicted in Figure S1.

Linear electrodes (LinMot E1200) enabled cyclic testing for normal and shear forces. V_{oc} data were captured via NI USB6356 and processed with a LabVIEW program. For robotic arm experiments, 16-channel V_{oc} data were collected via an STM-32 chip, transmitted to a Wi-Fi module via SPI, and wirelessly sent to mobile terminals for real-time LabVIEW interface control. The wireless acquisition circuit was designed using Altium Designer, with code developed in MDK-ARM.

https://doi.org/10.1021/acs.nanolett.4c00894
Nano Lett. 2024, 24, 5277−5283

Manipulator programming used Python, while the robotic arm's software was developed in VB.

■ ASSOCIATED CONTENT

Supporting Information

The Supporting Information is available free of charge at https://pubs.acs.org/doi/10.1021/acs.nanolett.4c00894.

Device's structure with layer details, output data images under various test conditions, cyclic stability test results, and deformation/potential distribution under stress states were analyzed via COMSOL Multiphysics. It theoretically analyzes the device's voltage output related to force direction and magnitude, deriving a corresponding formula. Additionally, it covers the device's voltage output during normal and shear force detection with a robotic arm system (PDF)

Video S1: simulation of mean deformation and potential of normal force (MP4)

Video S2: 3D diagram of contact potential change during press (MP4)

Video S3: shear force direction application of a contact point (MP4)

Video S4: normal force detection and application (MP4)

Video S5: shear force detection and application (MP4)

■ AUTHOR INFORMATION

Corresponding Authors

Zhong Lin Wang − *Beijing Institute of Nanoenergy and Nanosystems, Chinese Academy of Sciences, Beijing 101400, P. R. China; School of Nanoscience and Technology, University of Chinese Academy of Sciences, Beijing 100049, P. R. China*; orcid.org/0000-0002-5530-0380; Email: zhong.wang@mse.gatech.edu

Zhiyi Wu − *Beijing Institute of Nanoenergy and Nanosystems, Chinese Academy of Sciences, Beijing 101400, P. R. China; School of Nanoscience and Technology, University of Chinese Academy of Sciences, Beijing 100049, P. R. China*; orcid.org/0000-0002-3215-0092; Email: wuzhiyi@binn.cas.cn

Authors

Chengcheng Han − *Beijing Institute of Nanoenergy and Nanosystems, Chinese Academy of Sciences, Beijing 101400, P. R. China; School of Nanoscience and Technology, University of Chinese Academy of Sciences, Beijing 100049, P. R. China*

Zhi Cao − *Beijing Institute of Nanoenergy and Nanosystems, Chinese Academy of Sciences, Beijing 101400, P. R. China; School of Nanoscience and Technology, University of Chinese Academy of Sciences, Beijing 100049, P. R. China*

Yiran Hu − *Beijing Institute of Nanoenergy and Nanosystems, Chinese Academy of Sciences, Beijing 101400, P. R. China; School of Nanoscience and Technology, University of Chinese Academy of Sciences, Beijing 100049, P. R. China*

Zhiwei Zhang − *Beijing Institute of Nanoenergy and Nanosystems, Chinese Academy of Sciences, Beijing 101400, P. R. China; School of Nanoscience and Technology, University of Chinese Academy of Sciences, Beijing 100049, P. R. China*

Chengyu Li − *Beijing Institute of Nanoenergy and Nanosystems, Chinese Academy of Sciences, Beijing 101400, P. R. China; School of Nanoscience and Technology, University of Chinese Academy of Sciences, Beijing 100049, P. R. China*

Complete contact information is available at: https://pubs.acs.org/10.1021/acs.nanolett.4c00894

Author Contributions

Z.W. and Z.L.W. conceived the idea and supervised the experiment. C.H. and Z.C. prepared the manuscript. Y.H., Z.Z., and C.L. helped with the experiments. All of the authors discussed the results and commented on the manuscript and contributed to the manuscript preparation.

Funding

The research was supported by the National Key Research and Development (R&D) Program from Ministry of Science and Technology (2023YFB3208104).

Notes

The authors declare no competing financial interest.

■ ACKNOWLEDGMENTS

The authors thank the support of the National Key Research and Development (R&D) Program from Ministry of Science and Technology (2023YFB3208104).

■ REFERENCES

(1) Larson, C.; Peele, B.; Li, S.; Robinson, S.; Totaro, M.; Beccai, L.; Mazzolai, B.; Shepherd, R. Highly stretchable electroluminescent skin for optical signaling and tactile sensing. *Science* **2016**, *351* (6277), 1071−1074.

(2) Billard, A.; Kragic, D. Trends and challenges in robot manipulation. *Science* **2019**, *364* (6446), 8414.

(3) Rodriguez, A. The unstable queen: Uncertainty, mechanics, and tactile feedback. *Science Robotics* **2021**, *6* (54), 4667.

(4) Maheshwari, V.; Saraf, R. F. High-Resolution Thin-Film Device to Sense Texture by Touch. *Science* **2006**, *312* (5779), 1501−1504.

(5) Sundaram, S.; Kellnhofer, P.; Li, Y.; Zhu, J.-Y.; Torralba, A.; Matusik, W. Learning the signatures of the human grasp using a scalable tactile glove. *Nature* **2019**, *569* (7758), 698−702.

(6) Su, Q.; Zou, Q.; Li, Y.; Chen, Y.; Teng, S.-Y.; Kelleher, J. T.; Nith, R.; Cheng, P.; Li, N.; Liu, W.; Dai, S.; Liu, Y.; Mazursky, A.; Xu, J.; Jin, L.; Lopes, P.; Wang, S. A stretchable and strain-unperturbed pressure sensor for motion interference−free tactile monitoring on skins. *Science Advances* **2021**, *7* (48), 4563.

(7) Osborn, L. E.; Dragomir, A.; Betthauser, J. L.; Hunt, C. L.; Nguyen, H. H.; Kaliki, R. R.; Thakor, N. V. Prosthesis with neuromorphic multilayered e-dermis perceives touch and pain. *Science Robotics* **2018**, *3* (19), 3818.

(8) Zollo, L.; Di Pino, G.; Ciancio, A. L.; Ranieri, F.; Cordella, F.; Gentile, C.; Noce, E.; Romeo, R. A.; Dellacasa Bellingegni, A.; Vadalà, G.; Miccinilli, S.; Mioli, A.; Diaz-Balzani, L.; Bravi, M.; Hoffmann, K.-P.; Schneider, A.; Denaro, L.; Davalli, A.; Gruppioni, E.; Sacchetti, R.; Castellano, S.; Di Lazzaro, V.; Sterzi, S.; Denaro, V.; Guglielmelli, E. Restoring tactile sensations via neural interfaces for real-time force-and-slippage closed-loop control of bionic hands. *Science Robotics* **2019**, *4* (27), 9924.

(9) Wang, M.; Yan, Z.; Wang, T.; Cai, P.; Gao, S.; Zeng, Y.; Wan, C.; Wang, H.; Pan, L.; Yu, J.; Pan, S.; He, K.; Lu, J.; Chen, X. Gesture recognition using a bioinspired learning architecture that integrates visual data with somatosensory data from stretchable sensors. *Nat. Electron.* **2020**, *3* (9), 563−570.

(10) Yu, X.; Xie, Z.; Yu, Y.; Lee, J.; Vazquez-Guardado, A.; Luan, H.; Ruban, J.; Ning, X.; Akhtar, A.; Li, D.; Ji, B.; Liu, Y.; Sun, R.; Cao, J.; Huo, Q.; Zhong, Y.; Lee, C.; Kim, S.; Gutruf, P.; Zhang, C.; Xue, Y.; Guo, Q.; Chempakasseril, A.; Tian, P.; Lu, W.; Jeong, J.; Yu, Y.; Cornman, J.; Tan, C.; Kim, B.; Lee, K.; Feng, X.; Huang, Y.; Rogers, J. A. Skin-integrated wireless haptic interfaces for virtual and augmented reality. *Nature* **2019**, *575* (7783), 473−479.

(11) Ge, J.; Wang, X.; Drack, M.; Volkov, O.; Liang, M.; Cañón Bermúdez, G. S.; Illing, R.; Wang, C.; Zhou, S.; Fassbender, J.; Kaltenbrunner, M.; Makarov, D. A bimodal soft electronic skin for tactile and touchless interaction in real time. *Nat. Commun.* **2019**, *10* (1), 4405.
(12) Wang, X.; Dong, L.; Zhang, H.; Yu, R.; Pan, C.; Wang, Z. L. Recent Progress in Electronic Skin. *Advanced Science* **2015**, *2* (10), 1500169.
(13) Chortos, A.; Liu, J.; Bao, Z. Pursuing prosthetic electronic skin. *Nat. Mater.* **2016**, *15* (9), 937−950.
(14) Ramuz, M.; Tee, B. C. K.; Tok, J. B. H.; Bao, Z. Transparent, Optical, Pressure-Sensitive Artificial Skin for Large-Area Stretchable Electronics. *Adv. Mater.* **2012**, *24* (24), 3223−3227.
(15) Zeng, X.; Wang, Z.; Zhang, H.; Yang, W.; Xiang, L.; Zhao, Z.; Peng, L.-M.; Hu, Y. Tunable, Ultrasensitive, and Flexible Pressure Sensors Based on Wrinkled Microstructures for Electronic Skins. *ACS Appl. Mater. Interfaces* **2019**, *11* (23), 21218−21226.
(16) Kim, S.; Laschi, C.; Trimmer, B. Soft robotics: a bioinspired evolution in robotics. *Trends Biotechnol.* **2013**, *31* (5), 287−294.
(17) Sun, X.; Sun, J.; Li, T.; Zheng, S.; Wang, C.; Tan, W.; Zhang, J.; Liu, C.; Ma, T.; Qi, Z.; Liu, C.; Xue, N. Flexible Tactile Electronic Skin Sensor with 3D Force Detection Based on Porous CNTs/PDMS Nanocomposites. *Nano-Micro Letters* **2019**, *11* (1), 57.
(18) Viry, L.; Levi, A.; Totaro, M.; Mondini, A.; Mattoli, V.; Mazzolai, B.; Beccai, L. Flexible Three-Axial Force Sensor for Soft and Highly Sensitive Artificial Touch. *Adv. Mater.* **2014**, *26* (17), 2659−2664.
(19) Yan, Y.; Hu, Z.; Yang, Z.; Yuan, W.; Song, C.; Pan, J.; Shen, Y. Soft magnetic skin for super-resolution tactile sensing with force self-decoupling. *Science Robotics* **2021**, *6* (51), 8801.
(20) Sun, Q.-J.; Lai, Q.-T.; Tang, Z.; Tang, X.-G.; Zhao, X.-H.; Roy, V. A. L. Advanced Functional Composite Materials toward E-Skin for Health Monitoring and Artificial Intelligence. *Advanced Materials Technologies* **2023**, *8* (5), 2201088.
(21) Guo, W.-T.; Tang, X.-G.; Tang, Z.; Sun, Q.-J. Recent Advances in Polymer Composites for Flexible Pressure Sensors. *Polymers* **2023**, *15*, 2176.
(22) Lai, Q.-T.; Zhao, X.-H.; Sun, Q.-J.; Tang, Z.; Tang, X.-G.; Roy, V. A. L. Emerging MXene-Based Flexible Tactile Sensors for Health Monitoring and Haptic Perception. *Small* **2023**, *19* (27), 2300283.
(23) Qu, X.; Xue, J.; Liu, Y.; Rao, W.; Liu, Z.; Li, Z. Fingerprint-shaped triboelectric tactile sensor. *Nano Energy* **2022**, *98*, 107324.
(24) Gao, S.; Chen, J. L.; Dai, Y. N.; Wang, R.; Kang, S. B.; Xu, L. J. Piezoelectric-Based Insole Force Sensing for Gait Analysis in the Internet of Health Things. *IEEE Consumer Electronics Magazine* **2021**, *10* (1), 39−44.
(25) Zhang, W.; Xi, Y.; Wang, E.; Qu, X.; Yang, Y.; Fan, Y.; Shi, B.; Li, Z. Self-Powered Force Sensors for Multidimensional Tactile Sensing. *ACS Appl. Mater. Interfaces* **2022**, *14* (17), 20122−20131.
(26) Wang, Z.; Bu, T.; Li, Y.; Wei, D.; Tao, B.; Yin, Z.; Zhang, C.; Wu, H. Multidimensional Force Sensors Based on Triboelectric Nanogenerators for Electronic Skin. *ACS Appl. Mater. Interfaces* **2021**, *13* (47), 56320−56328.
(27) Boutry, C. M.; Negre, M.; Jorda, M.; Vardoulis, O.; Chortos, A.; Khatib, O.; Bao, Z. A hierarchically patterned, bioinspired e-skin able to detect the direction of applied pressure for robotics. *Science Robotics* **2018**, *3* (24), 6914.
(28) Yuan, F.; Wang, W.; Liu, S.; Zhou, J.; Wang, S.; Wang, Y.; Deng, H.; Xuan, S.; Gong, X. A self-powered three-dimensional integrated e-skin for multiple stimuli recognition. *Chem. Eng. J.* **2023**, *451*, 138522.
(29) Ren, Z.; Nie, J.; Shao, J.; Lai, Q.; Wang, L.; Chen, J.; Chen, X.; Wang, Z. L. Fully Elastic and Metal-Free Tactile Sensors for Detecting both Normal and Tangential Forces Based on Triboelectric Nanogenerators. *Adv. Funct. Mater.* **2018**, *28* (31), 1802989.
(30) Chen, J.; Yang, J.; Li, Z.; Fan, X.; Zi, Y.; Jing, Q.; Guo, H.; Wen, Z.; Pradel, K. C.; Niu, S.; Wang, Z. L. Networks of Triboelectric Nanogenerators for Harvesting Water Wave Energy: A Potential Approach toward Blue Energy. *ACS Nano* **2015**, *9* (3), 3324−3331.
(31) Feng, Y.; Zhang, L.; Zheng, Y.; Wang, D.; Zhou, F.; Liu, W. Leaves based triboelectric nanogenerator (TENG) and TENG tree for wind energy harvesting. *Nano Energy* **2019**, *55*, 260−268.
(32) Fang, Y.; Zou, Y.; Xu, J.; Chen, G.; Zhou, Y.; Deng, W.; Zhao, X.; Roustaei, M.; Hsiai, T. K.; Chen, J. Ambulatory Cardiovascular Monitoring Via a Machine-Learning-Assisted Textile Triboelectric Sensor. *Adv. Mater.* **2021**, *33* (41), 2104178.
(33) Zhao, X.; Askari, H.; Chen, J. Nanogenerators for smart cities in the era of 5G and Internet of Things. *Joule* **2021**, *5* (6), 1391−1431.
(34) Charalambides, A.; Bergbreiter, S. Rapid Manufacturing of Mechanoreceptive Skins for Slip Detection in Robotic Grasping. *Advanced Materials Technologies* **2017**, *2* (1), 1600188.
(35) Yamaguchi, T.; Kashiwagi, T.; Arie, T.; Akita, S.; Takei, K. Human-Like Electronic Skin-Integrated Soft Robotic Hand. *Advanced Intelligent Systems* **2019**, *1* (2), 1900018.
(36) Lin, Y.; Duan, S.; Zhu, D.; Li, Y.; Wang, B.; Wu, J. Self-Powered and Interface-Independent Tactile Sensors Based on Bilayer Single-Electrode Triboelectric Nanogenerators for Robotic Electronic Skin. *Advanced Intelligent Systems* **2023**, *5* (4), 2100120.
(37) Wang, Y.; Wu, H.; Xu, L.; Zhang, H.; Yang, Y.; Wang, Z. L. Hierarchically patterned self-powered sensors for multifunctional tactile sensing. *Science Advances* **2020**, *6* (34), 9083.
(38) Chen, H.; Miao, L.; Su, Z.; Song, Y.; Han, M.; Chen, X.; Cheng, X.; Chen, D.; Zhang, H. Fingertip-inspired electronic skin based on triboelectric sliding sensing and porous piezoresistive pressure detection. *Nano Energy* **2017**, *40*, 65−72.
(39) Zhu, M.; Sun, Z.; Zhang, Z.; Shi, Q.; He, T.; Liu, H.; Chen, T.; Lee, C. Haptic-feedback smart glove as a creative human-machine interface (HMI) for virtual/augmented reality applications. *Science Advances* **2020**, *6* (19), 8693.
(40) Han, C.; Cao, Z.; Yuan, Z.; Zhang, Z.; Huo, X.; Zhang, L. A.; Wu, Z.; Wang, Z. L. Hybrid Triboelectric-Electromagnetic Nanogenerator with a Double-Sided Fluff and Double Halbach Array for Wave Energy Harvesting. *Adv. Funct. Mater.* **2022**, *32* (36), 2205011.
(41) Cao, Z.; Yuan, Z.; Han, C.; Feng, J.; Wang, B.; Wang, Z. L.; Wu, Z. Hybrid Triboelectric−Electromagnetic Nanogenerator Based on a Tower Spring for Harvesting Omnidirectional Vibration Energy. *ACS Appl. Nano Mater.* **2022**, *5* (8), 11577−11585.
(42) Shan, C.; He, W.; Wu, H.; Fu, S.; Li, K.; Liu, A.; Du, Y.; Wang, J.; Mu, Q.; Liu, B.; Xi, Y.; Hu, C. Dual Mode TENG with Self-Voltage Multiplying Circuit for Blue Energy Harvesting and Water Wave Monitoring. *Adv. Funct. Mater.* **2023**, *33* (33), 2305768.